

Chapter 7

Secondary Anisotropies

*Mingled and merged, densely sprouting,
In the primaeval mass, there is no shape.
Spreading and scattering, leaving no trail behind,
In the darkness of its depths, there is no sound.*

—Chuang-tzu, 14

Between recombination and the present, astrophysical processes can alter the anisotropy spectrum. In general, they may have two distinct effects:

1. Erasure or masking of primary anisotropies by rescattering and other filtering.
2. Generation of secondary fluctuations imprinting the mark of a much more evolved and complex universe.

Indeed from the null result of the Gunn-Peterson test [69], we know that the universe is almost completely ionized out to redshift 4-5 [144, 172]. Although this alone would only have a percent or so affect on primary anisotropies, it raises the possibility that reionization of the universe could have occurred at a much higher redshift. In models with sufficient small scale power, it is plausible that an early round of structure formation may have released the energy required to keep the universe ionized at high redshift (see *e.g.* [58, 165]).

Early reionization scenarios enjoyed a brief period of popularity following the detection of puzzlingly small anisotropies at the $\sim 2^\circ$ scale by the SP91 experiment [145], as the great number of papers that it generated bears witness to [61, 45, 31, 75, 160, 81, 46]. Although the status is far from clear at the present, their popularity has declined due to the steady stream of higher detections on roughly the same scale [174, 104]. Still, some filtering

of primary anisotropies must have occurred. Indeed, for typical (primordial) isocurvature baryon (PIB) models [125, 126] significant reionization is both necessary and natural due to their excessive amounts of small scale power.

Since secondary anisotropies depend on the astrophysical details of structure formation, they provide interesting constraints on models and clues to the process of structure formation. On the other hand, they do not have much power to measure background parameters in a model independent manner. In this sense, primary and secondary anisotropies complement each other. If reionization is not too substantial, both mechanisms may contribute. In this case, the information contained in the CMB increases and consequently so does the care needed to extract it. The problem of extraction alone would motivate the study of secondary anisotropy formation (see also Appendix A.3).

In this chapter, we first discuss the general principles that govern secondary anisotropy formation in linear theory. Since the results are quite model dependent, we will offer the CDM and PIB models to illustrate their effect. Linear contributions are generally cancelled at small scales. It is therefore necessary to include higher order effects. We discuss second order calculations in detail and find that the Vishniac, or second order Doppler contribution is the dominant source at small angles. We then briefly survey highly non-linear effects and their importance for secondary anisotropy formation. In this case, even the qualitative sense of the effects can be model dependent.

7.1 Linear Contributions

7.1.1 Reionization Damping

Secondary anisotropy formation in linear theory follows the same basic principles as primary anisotropy formation. The main difference is that the photons and baryons are no longer tightly coupled. As shown in §5.3, the baryons are released from Compton drag when the redshift falls below

$$z_d \simeq 160(\Omega_0 h^2)^{1/5} x_e^{-2/5}, \quad (7.1)$$

where recall that x_e is the ionization fraction. Fluctuations in the matter then are free to grow and follow the pressureless solution D to the evolution equations (see §5.1). Likewise, the photon diffusion length grows to be comparable to the horizon size. Last scattering effectively occurs when the Compton scattering time becomes greater than the expansion

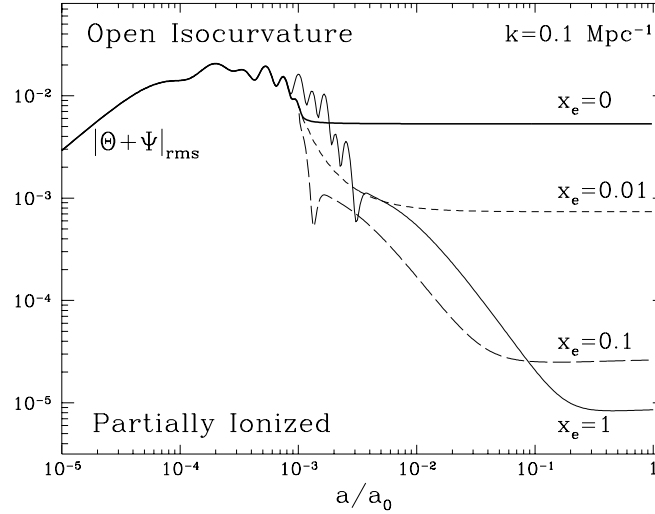


Figure 7.1: Reionization Damping Evolution

If the universe stays transparent after standard recombination at $z_* \simeq a_0/a_* \simeq 1000$, the acoustic oscillations in the photon-baryon fluid will be frozen into the rms temperature fluctuation. For partially reionized models, the diffusion length continues to grow and sharply damps the acoustic contributions. Fluctuations are regenerated by scattering induced Doppler shifts from the electrons. The model here is an open baryon isocurvature model with $\Omega_0 = \Omega_b = 0.2, h = 0.5$.

time. More specifically, we can define it as the epoch when optical depth reaches unity. Since the optical depth

$$\tau = 4.61 \times 10^{-2} (1 - Y_p/2) x_e \frac{\Omega_b h}{\Omega_0^2} \times \begin{cases} [2 - 3\Omega_0 + (1 + \Omega_0 z)^{1/2} (\Omega_0 z + 3\Omega_0 - 2)] & \Omega_\Lambda = 0 \\ \Omega_0 [1 - \Omega_0 + \Omega_0 (1 + z)^3]^{1/2} - \Omega_0 & \Omega_0 + \Omega_\Lambda = 1 \end{cases} \quad (7.2)$$

if x_e is constant, this occurs at

$$z_* \simeq 98 \left(\frac{\Omega_0 h^2}{0.25} \right)^{1/3} \left[\frac{(x_e \Omega_b h^2) (1 - Y_p/2)}{0.0125 \cdot 0.885} \right]^{-2/3}, \quad (7.3)$$

for both cases since last scattering occurs before curvature or Λ domination. Notice that last scattering occurs after the end of the drag epoch for sufficiently high ionization and baryon fraction.

In this limit, photons diffuse amongst the freely falling baryons inside the horizon. Recall that diffusion damps intrinsic photon fluctuations as $e^{-\tau}$ due to streaming conversion of inhomogeneities to anisotropies and subsequent rescattering isotropization. Thus

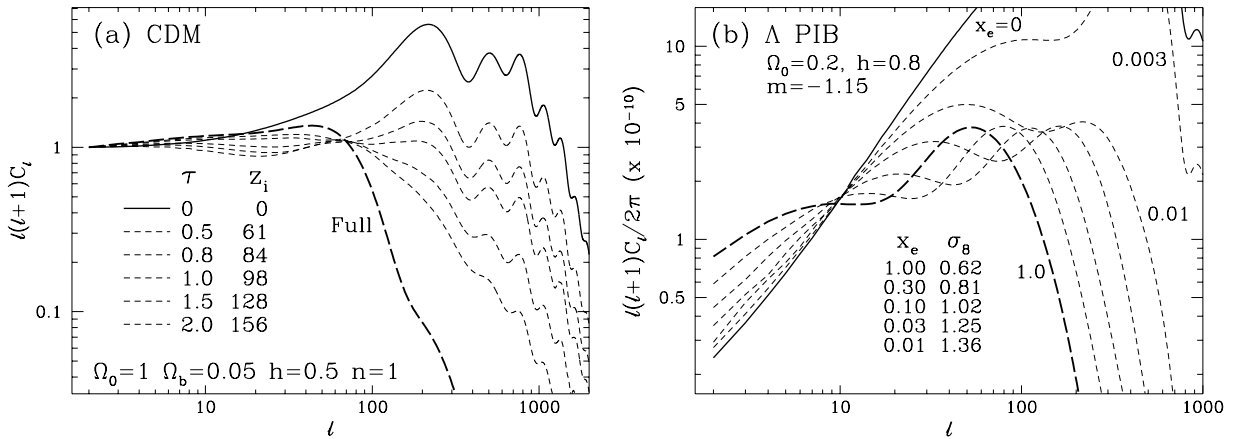


Figure 7.2: Reionization Damped Spectrum

(a) Standard CDM. Reionization damps anisotropy power as $e^{-2\tau}$ under the horizon (diffusion length) at last scattering. The models here are fully ionized $x_e = 1.0$ out to a reionization redshift z_i . Notice that with high optical depth, fluctuations at intermediate scales are regenerated as the fully ionized (long-dashed) model shows. (b) Λ PIB. PIB models have excess small scale power and require high optical depth to damp the corresponding anisotropy. In this case, both reionization damping and regeneration can be quite important and the spectrum is sensitive to the details of the ionization history not merely the optical depth. Models here have constant ionization from $z_i = 800$ and are normalized to the COBE detection [74]. Note that the amplitude of matter fluctuations σ_8 is also highly sensitive to the ionization.

primary anisotropies are sharply damped below the horizon scale implying that no acoustic oscillations will survive (see Fig. 7.1).

Features in the primary spectrum will be accordingly damped away as the optical depth between recombination and the present increases. For sufficiently high optical depth, the ability to measure fundamental cosmological parameters through the location of the peaks may be lost (see Fig. 7.2a). Notice that for $\tau \lesssim 1$, the oscillation amplitudes are still high enough to make measurements possible. Beyond this value, the primary signal is likely to be lost in the noise, foreground contamination, and non-linear source contributions. For the low $\Omega_b h^2 = 0.0125$ standard CDM model, this only occurs for an ionization redshift $z_i \gtrsim 100$. This possibility is highly unlikely since its $n = 1$ primordial spectrum does not have enough power for such early structure formation.

7.1.2 COBE Constraints on PIB Models

Reionization damping can on the other hand save models which would otherwise predict too high an amplitude for small scale anisotropies. Such is the case for standard PIB

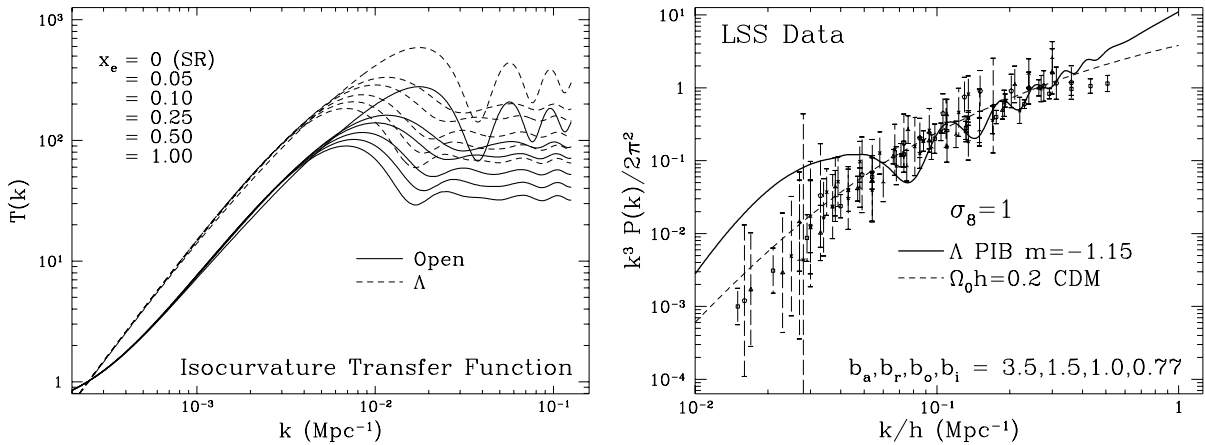


Figure 7.3: PIB Matter Power Spectrum

(a) Transfer function. Baryon perturbations $\Delta_b(\eta_0, k) = T(k)S(0, k)$ have a prominent peak at the maximal Jeans scale. Silk damping of acoustic oscillations increases with ionization leaving a constant small scale tail. The amplitude of the tail depends on the amount of time between the drag epoch and the present for fluctuations to grow as $D(a)$. The model here is $\Omega_0 = 0.2$, $h = 0.5$. (b) Large scale structure data with optical bias unity and relative biases chosen to best reconstruct the power spectrum [122] (see also Appendix B.4) require that the isocurvature index $m \simeq -1$. The model plotted is a $m = -1.15$ Λ PIB model with $\Omega_0 = 0.2$, $h = 0.8$ and $x_e = 0.1$ chosen to match $\sigma_8 = 1$ with a *COBE* normalization and not violate CMB constraints. A low $\Omega_0 h$ σ_8 normalized CDM model is shown for comparison.

models which have initial isocurvature fluctuations $|S(0, k)|^2 \propto k^m$ in a baryon-dominated $\Omega_0 = \Omega_b$ universe [125, 126]. Although $\Omega_0 = 0.1 - 0.3$ models, designed to satisfy dynamical estimates of the mass, consequently fail to satisfy nucleosynthesis constraints on the baryon density, astrophysical processes could alter light element abundances [58, 59]. Moreover since there is no *ab initio* mechanism for generating the required entropy perturbations, the index m is fixed by measurements of large scale structure today. Recall from §5.2.3 that isocurvature perturbations evolve such that below the photon diffusion scale, the initial entropy fluctuations become the density perturbations that seed large scale structure (see Fig. 7.3). The observed power spectrum of approximately $P(k) \propto k^{-1}$ at large scale structure scales [122] then implies an $m \simeq -1$ initial power law in the model. Numerical simulations which take into account non-linearities confirm this result [157]. At the largest scales, however, isocurvature conditions prevent the formation of potential perturbations leaving $k^3|\Phi|^2 \propto k^{3+m}$ which is steeply rising for $m = -1$. When normalized to the *COBE* DMR measurement, this leads to a steeply rising spectrum of anisotropies with effective slope $n_{\text{eff}} \simeq 2$. This model therefore has three difficulties to overcome

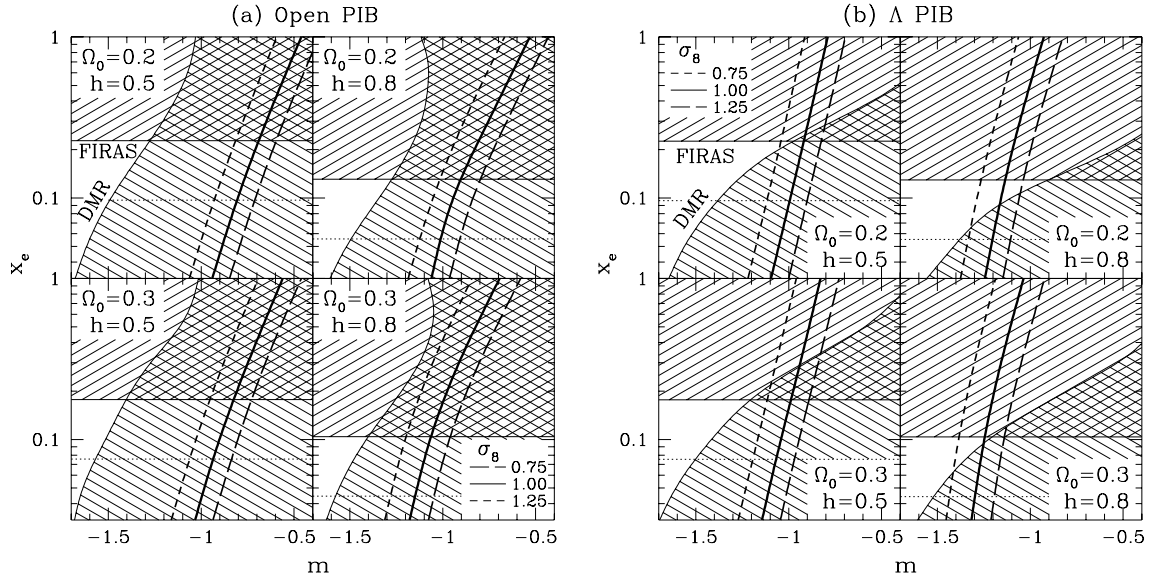


Figure 7.4: Constraints on PIB Models

The *COBE* DMR slope imposes a upper (95% confidence) limit on the initial spectral index m . The *COBE* FIRAS constraint on spectral distortions through the Compton- y parameter sets an upper limit on the ionization fraction. Here a conservative $T_e = 5000\text{K}$ is assumed with the more realistic $T_e = 10000\text{K}$ in dotted lines. The *COBE* DMR normalization also sets the level of matter fluctuations at the $8 h^{-1}\text{Mpc}$ scale σ_8 . (a) No open model simultaneously satisfies all the observational constraints. (b) For Λ models, a small region of parameter space is open for high h , low Ω_0 models.

1. Steeply rising *COBE* slope.
2. Large degree scale anisotropies.
3. High matter power spectrum normalization, σ_8 the amplitude at the $8h^{-1}\text{Mpc}$ scale.

They are all alleviated somewhat by reionization. Since Silk damping [150] does not destroy entropy fluctuations, the large amount of small scale power in the model allows for collapse of objects immediately following recombination (see §5.3.1). This could lead to sufficient energy input to reionize the universe as early as $z_i = 800$ [125, 126]. As we have noted, reionization damps the steeply rising primary signal (see Fig. 7.2b) and can help the first two problems. Furthermore, because Compton drag prevents the growth of structure, the ionization history can be tuned to provide the right ratio of matter to temperature fluctuations (see Figs. 5.6, 7.3).

Unfortunately, reionization can only damp fluctuations under the horizon scale at last scattering. Thus it is difficult to lower the effective slope n_{eff} at *COBE* scales $\ell \simeq 2 - 25$. Geodesic deviation carries the same physical scale onto smaller angles for open universes. Thus open models will thus be even less affected by reionization than Λ models. Smaller effects include raising the baryon content through $\Omega_b h^2$ which delays last scattering and increases the physical scale of the horizon. However even for flat models, the projection from the last scattering surface depends strongly on Ω_0 and counters the Ω_b dependence in these $\Omega_0 = \Omega_b$ baryonic models. Furthermore, the late ISW effect boosts the low order multipoles slightly as Ω_0 decreases (see §6.2.6). In the range of interest, decreasing Ω_0 leads to a shallower *COBE* slope. High x_e , high h , low Ω_0 , Λ models therefore offer the best prospects of bringing down the *COBE* slope.

The amount of reionization allowable is moreover constrained by the lack of spectral distortions in the CMB, $y \leq 2.5 \times 10^{-5}$ (95% CL) [116], where recall from §3.2.1 that $y = \int d\tau k(T_e - T)/m_e c^2$ measures the amount of upscattering in frequency from hot electrons. For collisional ionization, the electron temperatures must be quite high to overcome the Boltzmann suppression factor, typically $T_e \gtrsim 15000\text{K}$ [58, 28]. For photoionization, there is no firm lower limit on T_e since we can always fine tune the photoelectron energy to zero (*e.g.* with a decaying neutrino that produces 13.6 eV photons). Yet, given the ionization potential, we would generically expect electron energies of a few eV. Compton cooling from energy transfer to the CMB (see §3.1.2) then suppresses the equilibrium electron temperature to an average of $T_e \sim 5000\text{K}$ [165]. We will therefore adopt an electron temperature of $T_e = 5000\text{K}$. Since the collisionally ionized model is to date the only isocurvature scenario to successfully modify nucleosynthesis [58], this is a very conservative choice.

Bunn, Scott, & White [22] find that the observational constraints require $n_{\text{eff}} = 1.3_{-0.37}^{+0.24}$ (with quadrupole) which indicates that $n_{\text{eff}} = 2$ should be ruled out at greater than 95% confidence. Since PIB spectra are not pure power laws in the effective slope (see Fig. 7.2b), to quantify this constraint, we employ a full likelihood analysis of the two-year *COBE* DMR sky maps for open and Λ isocurvature baryon models fixed by Ω_0 , h , and x_e [74]. We expand the two-year DMR data in a set of basis functions which are optimized to have the maximum rejection power for incorrect models (see [21] for a full discussion). To set limits on m and the normalization Q , the rms quadrupole, we assume a prior distribution which is uniform for all Q and $m \leq 0$. Spectra with $m > 0$ are unphysical due to non-linear effects which regenerate an $m = 0$, $P(k) \propto k^4$ large scale tail to the fluctuations [124]. The

constraint in the crucial $m \simeq -1$ regime is not sensitive to the details of this cutoff. It is furthermore not very sensitive to ambiguities in the definition of power law initial conditions at the curvature scale (see §4.1.1 and §6.2.6 for a discussion). Shown in Fig. 7.4 are the 95% confidence upper limits imposed on m by integrating over the normalization Q to form the marginal likelihood in m . As expected, all open models with $m \simeq -1$ are ruled out regardless of ionization fraction, whereas highly ionized Λ models remain acceptable. Notice however that the constraint tightens for the highest ionization fractions. This is because fluctuations are in fact regenerated at the new last scattering surface if the optical depth is sufficiently high (see §7.1.3 below).

Since the PIB model is phenomenologically based, it is always possible to add free parameters to adjust the model to fit observations. Indeed an initial power spectrum with $m \simeq -1$ is required only in the large scale structure regime. Aside from simplicity arguments, we have no firm reason to believe that the power law behavior extends to *COBE* scales. It is therefore worthwhile to consider smaller scale anisotropy formation where CMB and large scale structure observations will overlap. This will eventually provide powerful consistency tests for *any* model since the two measure fluctuations at very different epochs in the evolution of structure (see *e.g.* [164]). In the case of early reionization, regeneration of small scale anisotropies can be significant. It is to this subject that we now turn.

7.1.3 Anisotropy Regeneration

Fluctuations are not entirely damped away by reionization (see Fig. 7.1). Since the baryons are in free fall after the drag epoch, they possess a non-negligible bulk velocity. Compton scattering still attempts to isotropize the photons in the electron rest frame and couples the photon and baryon bulk velocities V_γ and V_b . Thus at each scattering event, the photons are given a Doppler kick from the electrons. Subsequent diffusion over many wavelengths of the fluctuation damps away this contribution. Thus fluctuations will be on the order of $V_b \tau_k$ if the optical depth through a wavelength of the fluctuation, $\tau_k \simeq \dot{\tau}/k \ll 1$. In the opposite regime, the photons are still tightly coupled. Doppler fluctuations then go to V_b and add to the undamped temperature fluctuations.

We can employ analytic techniques to better understand these Doppler contributions. Ignoring curvature, as is appropriate for these small scales before last scattering, the

formal solution to the Boltzmann equation is

$$[\Theta + \Psi](\eta, k, \mu) = [\Theta + \Psi](\eta_d, k, \mu) e^{ik\mu(\eta_d - \eta)} e^{-\tau(\eta_d, \eta)} + [\Theta_D + \Theta_{ISW}](\eta, k, \mu), \quad (7.4)$$

where recall $k\mu = \mathbf{k} \cdot \boldsymbol{\gamma}$ and the optical depth $\tau(\eta_1, \eta_2) = \int_{\eta_1}^{\eta_2} \dot{\tau} d\eta$. Here Θ_D and Θ_{ISW} represent the Doppler and the ISW effect respectively. The initial conditions are taken at the drag epoch η_d so that we can consider the matter source V_b as evolving independently. As noted above, scattering rapidly damps out the contributions from before the drag epoch as $e^{-\tau}$, and we will hereafter ignore this term. Thus the photon temperature perturbation is a function of the matter perturbations alone. These source terms are explicitly given by

$$\begin{aligned} \Theta_D(\eta, k, \mu) &= \int_{\eta_d}^{\eta} (\Theta_0 + \Psi - i\mu V_b) \dot{\tau} e^{-\tau(\eta', \eta)} e^{ik\mu(\eta' - \eta)} d\eta', \\ \Theta_{ISW}(\eta, k, \mu) &= \int_{\eta_d}^{\eta} 2\dot{\Psi} e^{-\tau(\eta', \eta)} e^{ik\mu(\eta' - \eta)} d\eta', \end{aligned} \quad (7.5)$$

where we have neglected the small correction to the quadrupole from the angular dependence of Compton scattering (see [82] for the justification) and recall that the plane-wave decomposition is defined such that $\boldsymbol{\gamma} \cdot \mathbf{v}_b(\eta, \mathbf{x}) = -i\mu V_b(\eta, k) \exp(i\mathbf{k} \cdot \mathbf{x})$.

To solve equation (7.4) to the present, we must obtain an expression for the effective temperature $\Theta_0 + \Psi$ at last scattering. Taking the zeroth moment of equation (7.4), we obtain

$$[\Theta_0 + \Psi](\eta, k, \mu) = \int_{\eta_d}^{\eta} \dot{\tau} e^{-\tau(\eta', \eta)} \left\{ (\Theta_0 + \Psi + 2\dot{\Psi}) j_0[k(\eta - \eta')] - V_b j_1[k(\eta - \eta')] \right\} d\eta', \quad (7.6)$$

where we have employed the identity

$$j_\ell(z) = \frac{i^\ell}{2} \int_{-1}^1 \exp(i\mu z) P_\ell(\mu) d\mu, \quad (7.7)$$

with P_ℓ as the Legendre polynomial. In the diffusion limit, the optical depth across a wavelength is small and the sources do not vary much over a time scale $\eta \sim 1/k$. Taking these quantities out of the integral and assuming $\eta \gg \eta_d$, we obtain

$$[\Theta_0 + \Psi](\eta, k, \mu) \simeq [\Theta_0 + \Psi] \frac{\dot{\tau} \pi}{k} - V_b \frac{\dot{\tau} \pi}{k} + 2 \frac{\dot{\Psi} \pi}{k}, \quad (7.8)$$

where we have employed the relation

$$\int_0^\infty j_\ell(z) dz = \frac{\sqrt{\pi} \Gamma[(\ell + 1)/2]}{2 \Gamma[(\ell + 2)/2]}. \quad (7.9)$$

As advertised, the contribution from the electron velocity is of order $\dot{\tau}/k$ or the optical depth through a wavelength. It is thus suppressed at short wavelengths. Since last scattering occurs before curvature or Λ domination, the change in the potential across a wavelength is negligibly small and we can neglect the ISW contribution at last scattering. Therefore the effective temperature becomes

$$[\Theta_0 + \Psi](\eta, k, \mu) \simeq -V_b \frac{\dot{\tau}}{k} \quad (7.10)$$

through last scattering.

It may seem counterintuitive that a source to the dipole Θ_1 creates an isotropic temperature fluctuation Θ_0 . Mathematically, it is clear from the Boltzmann hierarchy (4.54) that the dipole indeed sources the monopole as photons travel across a wavelength, $k\delta\eta \sim 1$. Consider an observer at the origin of a sine wave baryon velocity fluctuation in real space $v_b(x) = V_b \sin(kx)$. The observer sees photons coming from both the crest at $kx = \pi/2$, where $v_b > 0$, and the trough at $kx = -\pi/2$, where $v_b < 0$. The scattered photon distribution at these sights will be oppositely aligned dipoles. Thus the scattered radiation observed at the origin will be *redshifted* in both directions. This leads to a net temperature fluctuation. Of course, the effect is not cumulative. Radiation from further crests and troughs have shifts that cancel leaving an effect only for the photons which scattered within a wavelength of the perturbation, $\Theta_0 = \mathcal{O}(V_b \dot{\tau}/k)$.

Although this contribution is suppressed at short wavelengths, it is comparatively important since the dipole source V_b itself is severely cancelled. Inserting the effective temperature (7.10) in equation (7.4) and integrating the dipole source by parts, we obtain

$$[\Theta + \Psi](\eta_0, k, \mu) = \int_{\eta_d}^{\eta_0} \frac{1}{k} (\dot{V}_b \dot{\tau} + V_b \ddot{\tau} + 2k \dot{\Psi}) e^{-\tau(\eta, \eta_0)} e^{ik\mu(\eta - \eta_0)} d\eta. \quad (7.11)$$

The multipole decomposition is then obtained from equation (7.7),

$$\frac{\Theta_\ell(\eta_0, k)}{2\ell + 1} = \int_{\eta_d}^{\eta_0} \frac{1}{k} [\dot{V}_b \dot{\tau} + V_b \ddot{\tau} + 2k \dot{\Psi}] e^{-\tau(\eta, \eta_0)} j_\ell[k(\eta_0 - \eta)] d\eta, \quad (7.12)$$

where we have employed equation (7.7) and recall that the multipole moments are defined such that $\Theta_\ell = i^\ell (2\ell + 1)^{\frac{1}{2}} \int_{-1}^1 P_\ell(\mu) \Theta d\mu$. For the open universe generalization, replace j_ℓ with X_ν^ℓ .

We can further simplify the result by noting that in the small scale limit the anisotropy is sourced over many wavelengths of the perturbation. Contributions from crests

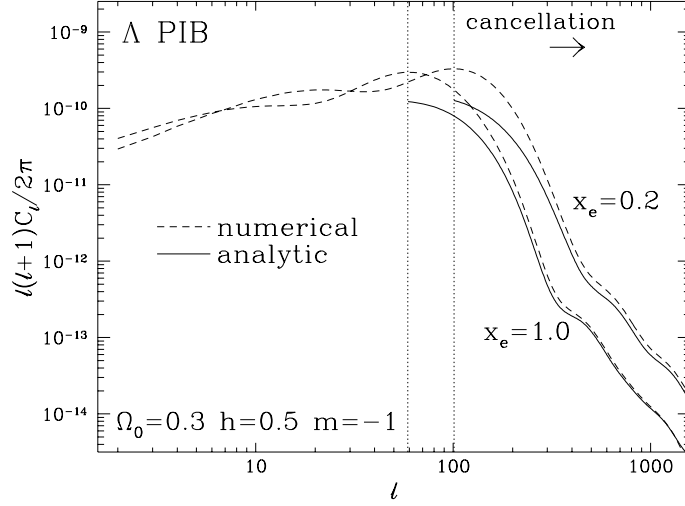


Figure 7.5: First Order Doppler Effect

Analytic calculations in the small scale cancellation regime show that first order anisotropies are dominated by the cancelled Doppler effect. Cancellation depends on the horizon scale at last scattering which increases with the ionization fraction x_e . As x_e or Ω_b is lowered, last scattering approaches the drag epoch where the analytic estimate breaks down.

and troughs of the perturbation cancel. In this case, $j_\ell(x)$ can be approximated as a δ -function at $x = \ell + 1/2$. In fact, we have already used this approximation for the late ISW effect of Λ models in §6.2.4. Employing equation (7.9) and the Stirling approximation of $\Gamma(x)/\Gamma(x + 1/2) \simeq x^{-1/2}$ for $x \gg 1$, we obtain

$$\frac{\Theta_\ell(\eta_0, k)}{2\ell + 1} \simeq \sqrt{\frac{\pi}{2\ell}} \frac{1}{k^2} \left[(\dot{V}_b \dot{\tau} + V_b \ddot{\tau} + 2k\dot{\Psi}) e^{-\tau(\eta, \eta_0)} \right] \Big|_{\eta=\eta_0-\ell/k}, \quad (7.13)$$

in a flat universe. With the relations

$$\begin{aligned} kV_b &= -\frac{\dot{D}}{D_0} \Delta_T(\eta_0, k), \\ k^2\Psi &= -\frac{3}{2} H_0^2 \Omega_0 \frac{D}{D_0} \frac{a_0}{a} \Delta_T(\eta_0, k), \end{aligned} \quad (7.14)$$

from the continuity and Poisson equations (5.24), the final expression for C_ℓ becomes

$$C_\ell^D = \frac{V}{\ell} \int \frac{dk}{k} \frac{1}{(k\eta_0)^6} S_L^2(\eta_0 - \ell/k) k^3 P(k), \quad (7.15)$$

where the matter power spectrum is $P(k) = |\Delta_T(\eta_0, k)|^2$ and the linear theory source is

$$S_L(\eta) = \left[\frac{\ddot{D}}{D_0} \dot{\tau} + \frac{\dot{D}}{D_0} \ddot{\tau} + 3H_0^2 \Omega_0 \frac{a_0}{a} \left(\frac{\dot{D}}{D_0} - \frac{D}{D_0} \frac{\dot{a}}{a} \right) \right] \eta_0^3 e^{-\tau(\eta, \eta_0)}. \quad (7.16)$$

This relation accurately describes the anisotropy on scales smaller than the horizon at last scattering if last scattering occurs *well* after the drag epoch (see Fig. 7.5). For low baryon fraction models such as CDM or partially ionized PIB models, these relations become less accurate. Notice that the amplitude of the Doppler effect depends strongly on the epoch of last scattering. This is due to the presence of a cancellation scale $k\eta_* \sim 1$ as we shall now see.

7.1.4 Cancellation Damping

It is instructive to consider the spatial power spectrum of the radiation $k^3|\Theta+\Psi|_{rms}^2$ as well as the anisotropy spectrum. With the projection deconvolved, the physical processes are easier to understand. In fact, historically the above analysis was originally presented in k -space [94]. The photons illuminate a surface of thickness $\delta\eta$ of the source field, *i.e.* the line of sight electron velocity for the Doppler effect and the decaying potential for the ISW effect. For perturbations with wavelength smaller than the thickness, the observer sees through many crests and troughs if the wavevector is aligned parallel to the line of sight. Thus contributions will be severely cancelled for these modes (see Figs. 1.7 and 1.9). A loophole occurs however if the wavevector is aligned perpendicular to the line of sight. In this case, all the contributions are additive along the line of sight and cancellation does not occur. For an isotropic source field, the net effect after summing over both components is a suppression of power by $(k\delta\eta)^{-1}$ or approximately the inverse number of wavelengths across the fluctuation.

For the Doppler effect, the source field is not isotropic. Indeed, it is only the line of sight component of the velocity that contributes at all. In linear theory, the potential gradient $\nabla\Psi$ generates an infall velocity. Thus gravitationally induced flows are irrotational $\nabla \times \mathbf{v}(\mathbf{x}) = 0$ or $\mathbf{k} \times \mathbf{v}(\mathbf{k}) = 0$ and the velocity is parallel to the wavevector. The line of sight component of the electron velocity vanishes for the perpendicular mode. In this case, cancellation is much more severe. Only if the electron velocity or the probability of scattering changes across a wavelength do the redshifts and blueshifts from crests and troughs not entirely cancel. The contributing sources are of order \dot{V}_b/k and $V_b\dot{\tau}/\dot{\tau}$, as we have seen, and suppress the net effect by an additional $(k\delta\eta)^{-2}$ in power.

We can formalize these considerations by noting that equation (7.11) is approximately a Fourier transform in η whose transform pair is $k\mu$ (with k fixed). This implies the

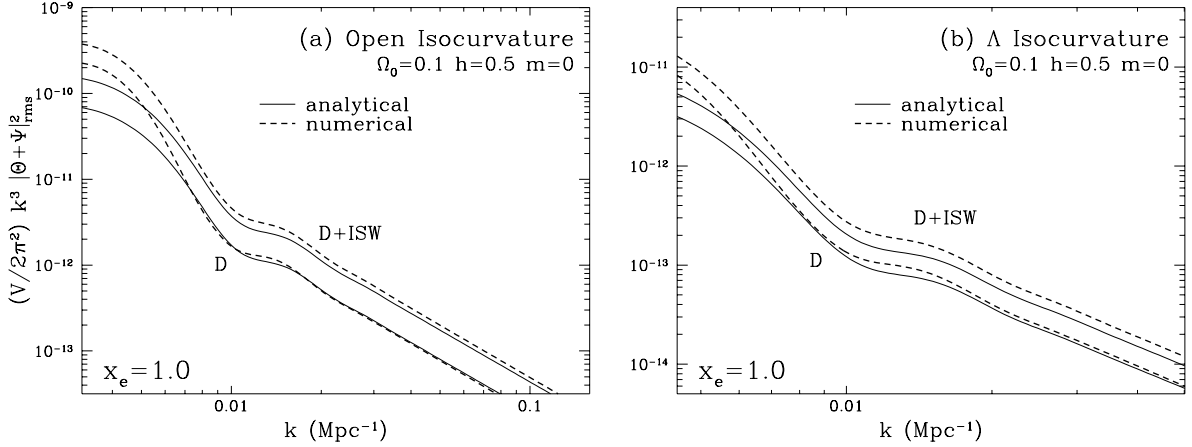


Figure 7.6: Cancellation Damping

If the wavelength is much smaller than the thickness of the surface upon which the anisotropy source lies, cancellation of contributions as the photon streams over many wavelengths of the perturbation will damp the effect. For the spatial power spectrum this implies mild cancellation of the late ISW effect and severe cancellation of the Doppler effect. The two can be comparable at small scales. For the Λ model however the projection carries the late ISW effect to larger angles where it is hidden by the Doppler effect in C_ℓ .

relation

$$k^2 \eta_0^3 \frac{[\Theta + \Psi](\eta_0, k, k\mu)}{\Delta_T(\eta_0, k)} \xrightarrow{\text{FT}} S_L(\eta), \quad (7.17)$$

where S_L is the linear theory source given by equation (7.16). Thus the two mean squares are related by Parseval's theorem,

$$\int_0^{\eta_0} S_L^2(\eta) d\eta \simeq \frac{1}{2\pi} k^4 \eta_0^6 P^{-1}(k) \int k d\mu |\Theta + \Psi|^2 \quad (7.18)$$

or rearranging the terms,

$$|\Theta + \Psi|_{rms}^2(\eta_0, k) \simeq \pi \frac{P(k)}{(k\eta_0)^5} \int_0^{\eta_0} S_L^2(\eta) d\eta / \eta_0. \quad (7.19)$$

where we have employed the relation $|\Theta + \Psi|_{rms}^2 = \frac{1}{2} \int_{-1}^1 d\mu |\Theta + \Psi|^2$.

All the terms in equation (7.19) are easy to understand. The velocity power spectrum is proportional to $P(k)/k^2$ and the potential power spectrum to $P(k)/k^4$. The Doppler term suffers cancellation in power by k^{-3} and the late ISW effect by k^{-1} . This brings the contribution to $P(k)/k^5$ for both effects and represents a significant small scale suppression compared with the matter fluctuations. In Fig. 7.6, we show an isocurvature baryon examples compared with the numerical results. Notice that the late ISW effect

can make a strong contribution to this *spatial* power spectrum even at small scales [80]. Equation (7.19) is slightly less accurate for the Λ late ISW effect since the potential is still decaying at the present and Parseval's theorem begins to break down because of the upper limit of the integral.

In fact, the radiation power spectrum can be approximated by taking a projection of real space onto angles

$$\frac{\ell(2\ell + 1)}{4\pi} C_\ell \simeq \frac{V}{2\pi^2} k_{\text{proj}}^3 |\Theta + \Psi|_{rms}^2(\eta_0, k_{\text{proj}}) \quad (7.20)$$

where $k_{\text{proj}} \simeq \ell/r_\theta(\eta_{\text{max}})$, η_{max} is the epoch when the source S_L peaks, and the angle-distance relation r_θ is given by equation (6.15). This is often useful for open universes where the radial eigenfunctions at high wavenumber are difficult to compute. However, one must be careful to separate component effects if S_L is bimodal. For example, since the Λ late ISW effect arises near the present time, spatial scales are carried to larger angles by the projection than for the Doppler contributions. In fact, even for the $\Omega_0 = 0.1$ Λ model, the late ISW effect is not visible in C_ℓ . This exhibits one of the dangers of naively working with spatial power spectra.

7.1.5 Minimal PIB Anisotropies

As an example of the regeneration of fluctuations through the Doppler effect, let us consider the open PIB model. It is particularly interesting to construct one with minimal anisotropies. We have seen that the steeply rising spectrum of anisotropies in this model can only be moderately mitigated by reionization because of the angle to distance relation in open universes. On the other hand, the lack of information about the initial spectrum near the curvature scale can be employed to evade the large angle constraint of §7.1.2. Degree scale anisotropies can alternately be employed to constrain the model. Since the observational state is still in flux, we shall limit ourselves to stating rules of thumb which may be useful to model builders in the future. For a concrete use of current data sets along these lines, see [81].

We might generalize the standard PIB model with a two dimensional parameterization of the ionization history involving both the ionization fraction x_e and the ionization redshift z_i . Since the fundamental scale for cancellation damping is the horizon at last scattering, anisotropies will depend sensitively on the epoch of last scattering. Raising the ionization fraction delays last scattering and makes the damping scale larger. By allowing

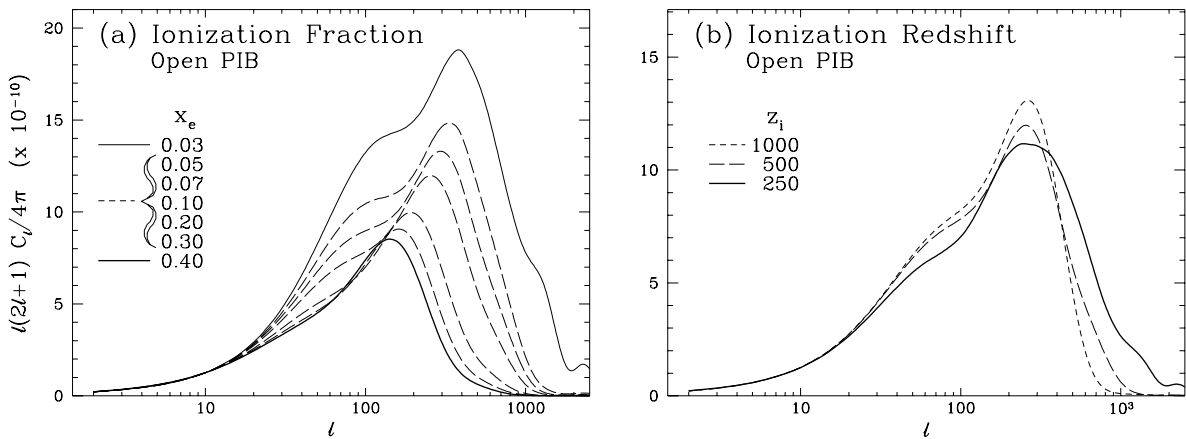


Figure 7.7: Minimal PIB Anisotropies

Two free parameters in the standard PIB model are the ionization fraction x_e and the ionization redshift z_i . (a) The ionization fraction, assumed to be constant after redshift $z_i = 500$, fixes the epoch of last scattering and the amount of cancellation damping. Aside from a small boost due to fluctuation growth, later last scattering always leads to smaller anisotropies. (b) The ionization redshift determines fluctuation growth before last scattering. Here $x_e = 0.1$. Adiabatic photon growth at large scales and baryon velocity growth at small scales yield opposite tendencies with z_i . The model here is open PIB with $\Omega_0 = 0.2$ $h = 0.5$ and $m = -0.5$. Ionization parameters are chosen to avoid Compton- y constraints.

more growth between the drag and last scattering epochs, it also increases the amplitude of velocity perturbations at last scattering. These two effects oppose each other but are not of equal magnitude: cancellation damping is more significant than growth (see Fig. 7.7). Thus minimal anisotropies will occur for maximal ionization fraction x_e .

The ionization redshift has a more complicated effect. Before reionization, fluctuations can grow in pressureless linear theory. Thus the baryon velocity and correspondingly the Doppler effect will be lowest for the latest reionization. However, at scales near to and above the horizon at last scattering, adiabatic growth of the temperature fluctuation dominates (see §5.1). For these scales, the latest reionization that still permits significant optical depth between recombination and the present minimizes fluctuations (see Fig. 7.7). Since PIB models must have high optical depth $\tau \gtrsim 3$ between recombination and the present to damp the large primary fluctuations [81], the ionization redshift must be significantly before last scattering. However, it must also be low enough to avoid Compton- y constraints. These constraints together with degree scale anisotropy and large scale structure observations will make PIB model building a real challenge in the future.

7.2 Second Order Contributions

The severe but in some sense “accidental” cancellation of the linear effect for reionized scenarios leads to the possibility that higher order effects may dominate sub-degree scale anisotropies. In this section, we will consider anisotropy generation to second order in perturbation theory [82, 46]. The fundamental equations and concepts necessary to understand these effects have already been discussed in §2.2.2. Applying them to the case of reionized models, we find that one source, the so-called Vishniac term [121, 169], dominates over all other contributions.

7.2.1 Generalized Doppler Effect

As we have seen, cancellation is a geometric effect and its severity for the Doppler effect is due irrotational nature of flows in linear theory. All modes except those for which \mathbf{k} is perpendicular to the line of sight are cancelled as the photon streams through many wavelengths of the perturbation to the observer. However for the Doppler effect, only the parallel component of the electron velocity yields an effect. Thus, for irrotational flows $\mathbf{v}_b \parallel \mathbf{k}$, Doppler contributions are severely suppressed. Note however that the full Doppler source is in fact $\dot{\tau} \mathbf{v}_b$, where recall $\dot{\tau} = x_e n_e \sigma_T a / a_0$, since the probability of scattering must be factored in. A photon is more likely to scatter in regions of high density or ionization. Thus perturbations in x_e and n_e will change the Doppler source. The effective velocity is therefore

$$\begin{aligned} \mathbf{q}(\mathbf{x}) &= [1 + \delta n_e(\mathbf{x})/n_e][1 + \delta x_e(\mathbf{x})/x_e] \mathbf{v}_b(\mathbf{x}) \\ &= [1 + \Delta_b(\mathbf{x})][1 + \delta x_e(\mathbf{x})/x_e] \mathbf{v}_b(\mathbf{x}). \end{aligned} \quad (7.21)$$

If fluctuations in the electron density or ionization are small, the additional contributions will be of second order. They can however escape the severe cancellation of the first order term. For example, there could be a large scale bulk flow $\mathbf{v}_b(k_1)$ with $\mathbf{k}_1 \parallel \boldsymbol{\gamma}$ and a small scale density fluctuation $\Delta_b(k_2)$ with $\mathbf{k}_2 \perp \boldsymbol{\gamma}$. In this case, scattering will induce a small scale temperature fluctuations perpendicular to the line of sight since more photons will have been scattered in the overdense regions (see Fig. 1.10). In the extreme limit of high density fluctuations, this is the kinetic Sunyaev-Zel’dovich effect for clusters (see §7.3 and [162]).

The solution of equation (7.4) can be generalized to

$$[\Theta + \Psi](\eta_0, \mathbf{k}, \boldsymbol{\gamma}) = \int_{\eta_a}^{\eta_0} \dot{\tau} e^{-\tau(\eta, \eta_0)} \boldsymbol{\gamma} \cdot \mathbf{q} e^{ik\mu(\eta - \eta_0)} d\eta. \quad (7.22)$$

We have neglected the feedback term into the temperature fluctuation at last scattering since it is suppressed by the optical depth through a wavelength. Following Vishniac [169], let us decompose the solution into multipole moments,

$$[\Theta + \Psi](\eta_0, \mathbf{k}, \boldsymbol{\gamma}) = \sum_{\ell, m} a_{\ell m}(\mathbf{k}) Y_{\ell m}(\Omega), \quad (7.23)$$

so that

$$|a_{\ell m}|^2 = \left| \int d\Omega Y_{\ell m}(\Omega) \int_0^{\eta_0} \dot{\tau} e^{-\tau(\eta, \eta_0)} (\boldsymbol{\gamma} \cdot \mathbf{q}) e^{ik\mu(\eta - \eta_0)} \right|^2. \quad (7.24)$$

Since the final result after summing over \mathbf{k} modes has no preferred direction, let us average over m such that $|a_\ell|^2 = \frac{1}{2\ell+1} \sum_m |a_{\ell m}|^2$, which corresponds to $|a_\ell|^2 = 4\pi |\Theta_\ell / (2\ell + 1)|^2$. Choosing $\hat{\mathbf{z}} \parallel \mathbf{k}$, we note that the azimuthal angle dependence separates out components of \mathbf{q} parallel and perpendicular to \mathbf{k} by employing the angular addition formula

$$\begin{aligned} \frac{4\pi}{2\ell + 1} \sum_m Y_{\ell m}^*(\theta, \phi) Y_{\ell m}(\theta', \phi') &= P_\ell(\cos\theta) P_\ell(\cos\theta') \\ &+ 2 \sum_m \frac{(\ell - m)!}{(\ell + m)!} P_\ell^m(\cos\theta) P_\ell^m(\cos\theta') \cos[m(\phi - \phi')]. \end{aligned} \quad (7.25)$$

Since $\boldsymbol{\gamma} \cdot \mathbf{q} = \cos\phi \sin\theta q_\perp + \cos\theta q_\parallel$, the cross terms between the two components vanish after integrating over azimuthal angles. The two contributions add in quadrature and may be considered as separate effects.

We have already noted that the $\mathbf{q} \parallel \mathbf{k}$ term is strongly suppressed by cancellation. Thus let us calculate the perpendicular component,

$$|a_\ell(k)|^2 = \frac{\pi}{2\ell(\ell + 1)} \left| \int_{-1}^1 d\mu P_\ell^1(1 - \mu^2)^{1/2} \int_0^{\eta_0} d\eta \dot{\tau} e^{-\tau(\eta, \eta_0)} q_\perp e^{ik\mu(\eta - \eta_0)} \right|^2. \quad (7.26)$$

The μ integral can be performed with the following identity

$$\int_{-1}^1 d\mu (1 - \mu^2)^{1/2} P_\ell^1(\mu) e^{iq\mu} = -2\ell(\ell + 1) (-i)^{-\ell+1} j_\ell(q)/q, \quad (7.27)$$

so that

$$|a_\ell(k)|^2 = 2\pi\ell(\ell + 1) \left| \int_0^{\eta_0} d\eta \dot{\tau} e^{-\tau(\eta, \eta_0)} q_\perp \frac{j_\ell(k\Delta\eta)}{k\Delta\eta} \right|^2, \quad (7.28)$$

where $\Delta\eta = \eta_0 - \eta$. Notice that this has a simple physical interpretation. We know from the spherical decomposition that a plane wave perturbation projects onto the shell at

distance $\Delta\eta$ as $j_\ell(k\Delta\eta)$. If the amplitude of the plane wave has an angular dependence, the projection is modified. In particular, the perpendicular component suffers less projection aliasing (see Fig. 1.7) and thus the higher oscillations are damped as $\eta/k\Delta\eta$.

7.2.2 Vishniac Effect

The Vishniac effect [121, 169] is the second order Doppler effect due to the density enhancement $n_e(\mathbf{x}) = \bar{n}_e[1 + \Delta_b(\mathbf{x})]$ in linear theory, *i.e.* $\mathbf{q}(\mathbf{x}) = [1 + \Delta(\mathbf{x})]\mathbf{v}_b(\mathbf{x})$ to second order. The convolution theorem tells us that

$$\mathbf{q}_\perp(\mathbf{k}) = \left(I - \frac{\mathbf{k}\mathbf{k}}{k^2}\right) \frac{1}{2} \sum_{\mathbf{k}'} \mathbf{v}_b(\mathbf{k}') \Delta_b(|\mathbf{k} - \mathbf{k}'|) + \mathbf{v}_b(\mathbf{k} - \mathbf{k}') \Delta_b(k'). \quad (7.29)$$

Taking the ensemble average of the fluctuation and assuming random phases for the underlying linear theory perturbations, we obtain

$$\langle q_\perp^*(k, \eta) q_\perp(k, \eta') \rangle = \frac{1}{2} \dot{D}(\eta) D(\eta) \dot{D}(\eta') D(\eta') \sum_{k'} d^2 P(k') P(|\mathbf{k} - \mathbf{k}'|), \quad (7.30)$$

where the projected vector

$$\mathbf{d} \equiv \left(I - \frac{\mathbf{k}\mathbf{k}}{k^2}\right) \left[\frac{\mathbf{k}'}{k^2} + \frac{\mathbf{k} - \mathbf{k}'}{|\mathbf{k} - \mathbf{k}'|^2} \right]. \quad (7.31)$$

A bit of straightforward but tedious algebra yields

$$\langle |a_\ell(k)|^2 \rangle = \frac{1}{4\pi} \frac{V}{\eta_0^3} \frac{\ell(\ell+1)}{k\eta_0} M_V(k) I_\ell^2(k) P^2(k), \quad (7.32)$$

where the mode-coupling integral is

$$M_V(k) = \int_0^\infty dy \int_{-1}^1 d(\cos\theta) \frac{(1 - \cos^2\theta)(1 - 2y\cos\theta)^2}{(1 + y^2 - 2y\cos\theta)^2} \frac{P[k(1 + y^2 - 2y\cos\theta)^{1/2}]}{P(k)} \frac{P(ky)}{P(k)}, \quad (7.33)$$

and the time integral is

$$\begin{aligned} I_\ell(k) &= \int_0^{\eta_0} \frac{d\eta}{\eta_0} S_V(\eta) j_\ell(k\Delta\eta) \\ &\simeq \sqrt{\frac{\pi}{2\ell}} \frac{1}{k\eta_0} S_V(\eta_0 - \ell/k), \end{aligned} \quad (7.34)$$

with

$$S_V(\eta) = \frac{\dot{D}}{D_0} \frac{D}{D_0} \frac{\eta_0^3}{\eta_0 - \eta} \dot{\tau} e^{-\tau}. \quad (7.35)$$

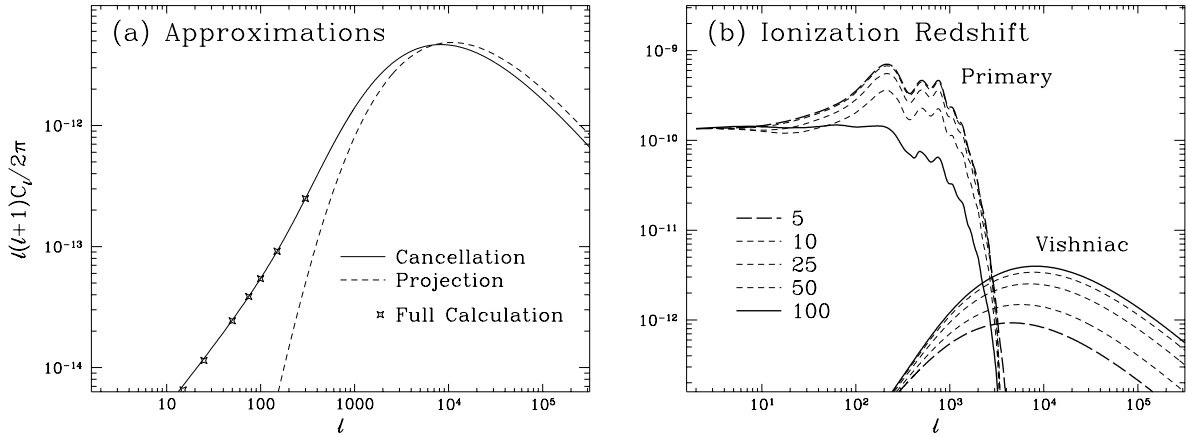


Figure 7.8: Vishniac Effect

The model is standard CDM $\Omega_0 = 1$, $\Omega_b = 0.05$, $h = 0.5$ with a quadrupole normalization to *COBE* of $20\mu\text{K}$. (a) The cancellation approximation to the Vishniac source is excellent. Calculations in k space projected onto angles underestimates the coherence angle of the Vishniac effect if fluctuations are all considered to come from last scattering $\eta_{max} = \eta_*$ in equation (7.20). (b) The Vishniac effect originates mainly after last scattering. Therefore even if the optical depth is as low as its Gunn-Peterson minimal value $z_i \simeq 5$, the Vishniac effect contributes a significant fraction of its total. Both primary anisotropies and the Vishniac effect may be present in the spectrum.

The random phase assumption for the underlying linear perturbations assures us that there are no cross terms between first and second order contributions or different k modes. Thus total anisotropy is obtained by integrating over all k modes [86],

$$\begin{aligned}
 C_\ell^V &= \frac{V}{2\pi^2} \int \frac{dk}{k} k^3 \langle |a_\ell(k)|^2 \rangle \\
 &= \frac{\ell(\ell+1)V^2}{(2\pi)^3 \eta_0^6} \int \frac{dk}{k} (k\eta_0)^2 M_V(k) I_\ell^2(k) P^2(k) \\
 &\simeq \frac{\ell}{(4\pi)^2} \frac{V^2}{\eta_0^6} \int \frac{dk}{k} M_V(k) S_V^2(\eta_0 - \ell/k) P^2(k).
 \end{aligned} \tag{7.36}$$

In Fig. 7.8, we plot the Vishniac effect for standard CDM. Notice that since S_V^2 depends on the amplitude of fluctuations to the fourth power, contributions are highly weighted toward late times and allows extremely small scales to contribute to observable anisotropies. Thus even with minimal ionization of $z_i = 5$, for which primary anisotropies are only damped at the percent level, the Vishniac effect can dominate the anisotropy at small scales.

Again it is useful to consider the k -space power spectrum. Employing the same

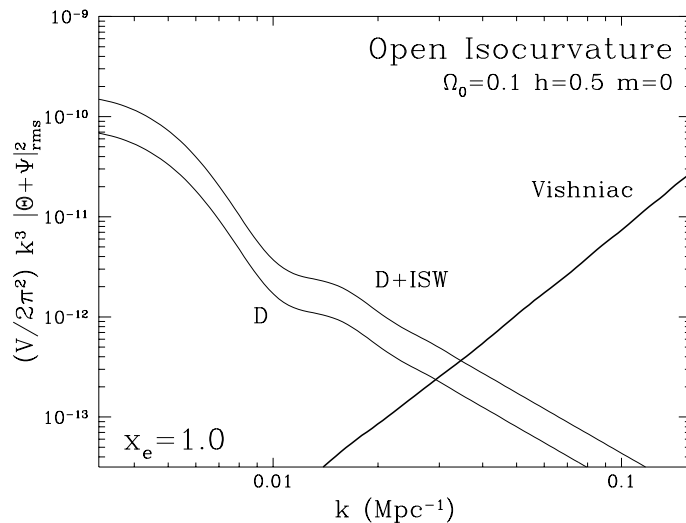


Figure 7.9: PIB Vishniac Power Spectrum

Analytic k space power spectrum calculation of the Vishniac effect in a PIB model. Vishniac contributions dominate over first order effects at small scales. For this steeply small scale weighted $m = 0$ spectrum, high k modes can contribute to lower ℓ modes that one would naively think. A full non-linear calculation is needed to account for these high k contributions.

Parseval approximation as for the first order contribution, we obtain

$$|\Theta + \Psi|^2 = \frac{V}{\eta_0^3} \frac{P^2(k)}{16\pi} M_V(k) \int_0^{\eta_0} (1 - \eta/\eta_0)^2 S_V^2(\eta) d\eta/\eta_0, \quad (7.37)$$

where the extra factor $1 - \eta/\eta_0$ in the integrand is due to the projection effect for the perpendicular mode. The k factors come from weak cancellation of $(k\delta\eta)^{-1}$, the continuity equation conversion of velocity to density $(k\eta)^{-2}$, and the volume in k available for mode coupling k^3 . Although the exact nature of the mode coupling integral can change the scaling, this simple power counting implies that the Vishniac effect will have more power at small scales than the cancelled first order contribution.

The k -space power spectrum has often been used in the past to estimate the anisotropy through a distance to angle conversion such as equation (7.20). The common assumption is that the Vishniac effect projects as if it all arises from the last scattering surface [50, 82, 46]. Given the strong weighting toward late times, this significantly underestimates its coherence scale (see Fig. 7.8a). The magnitude of this misestimation increases with the amount of small scale power in the model. Take for example, a PIB model with a steeply blue $m = 0$ spectrum (see Fig. 7.9). In this case, the k space power keeps on rising

to small scales. When this is projected onto ℓ space, it predicts a divergent anisotropy. Of course, second order theory breaks down as the fluctuation amplitude becomes comparable to unity so that the real spectrum would not continue to rise indefinitely. By inserting a cut-off at the non-linear scale, the anisotropy predicted by equation (7.36) or power projection is finite. However, to calculate the effect precisely, one needs to go to N -body simulations to accurately track the non-linear evolution.

7.2.3 Other Second Order Effects

It is by no means obvious that the Vishniac effect dominates over all other second order sources. It is therefore worthwhile to consider the general Boltzmann equation to second order [82]. Indeed spatial variations in the ionization fraction $\delta x_e(\mathbf{x})$ from patchy reionization can have an effect comparable to the Vishniac source. However because it is strongly dependent on the model for structure formation and reionization, it is beyond the scope of this discussion.

The second order Boltzmann equation is obtained by integrating the sources calculated in §2.2.2 over frequency and is given in real space by

$$\dot{\Theta} + \dot{\Psi} + \gamma^i \partial_i (\Theta + \Psi) = \dot{\tau} (1 + \Delta_b) \left[\Theta_0 + \Psi - \Theta + \gamma_i v_b^i - v_b^2 + 7(\gamma_i v_b^i)^2 \right] \quad (7.38)$$

$$+ 2\dot{\Psi} + \mathcal{O}([\Theta_0 - \Theta]v_b)], \quad (7.39)$$

where we have again neglected the small correction to the quadrupole [82]. We also assume that the ionization is uniform. Aside from the $\mathcal{O}(\Delta_b v_b)$ Vishniac contribution, there are several new terms to consider here.

$\mathcal{O}(v_b^2)$ Quadratic Doppler Effect

The kinetic energy of the electrons can be transferred to the photons in a manner identical to the thermal energy transfer of the Sunyaev-Zel'dovich effect (see §2.2.2 and §7.3). Spatial variations in the kinetic energy cause of order v_b^2 anisotropies in the CMB. Note that these anisotropies carry spectral distortions of the Compton- y just as their thermal counterpart.

These fluctuations do not suffer the drastic cancellation of the linear Doppler effect since the energy is direction independent. At small scales, the power is reduced by a factor $(k\delta\eta)^{-1}$ like the late ISW and Vishniac effect. Counting powers in k , we expect that aside

from a spectrum-dependent mode-coupling integral, the contribution will consist of $(k\delta\eta)^{-1}$ from cancellation, $(k\eta)^{-4}$ from the velocity to density conversion, and k^3 for the volume available to mode coupling. This gives a total of k^{-2} and implies that the Vishniac effect should be more important at small scales.

The Parseval approximation to the power spectrum confirms this scaling relation,

$$|\Theta + \Psi|_{rms}^2 = \frac{1}{32\pi} \frac{V}{\eta_0^3} \frac{1}{(k\eta_0)^2} M_Q(k) P^2(k) \int_0^{\eta_0} S_Q^2(\eta) d\eta / \eta_0, \quad (7.40)$$

where the mode-coupling integral is

$$M_Q(k) = \int_0^\infty dy \int_{-1}^{+1} d(\cos\theta) \frac{(y - \cos\theta)^2 - 7(1 - \cos^2\theta)(y - \cos\theta)y + \frac{147}{8}(1 - \cos^2\theta)^2 y^2}{(1 + y^2 - 2y \cos\theta)^2} \\ \times \frac{P[k(1 + y^2 - 2y \cos\theta)^{1/2}]}{P[k]} \frac{P[ky]}{P[k]}, \quad (7.41)$$

and the source is

$$S_Q(\eta) = \frac{\dot{D}}{D_0} \frac{\dot{D}}{D_0} \dot{\tau} e^{-\tau(\eta, \eta_0)} \eta_0^3. \quad (7.42)$$

Therefore, unless the mode-coupling integral behaves much differently than its Vishniac counterpart, this contribution will be small in comparison. In Fig. 7.10, we show a comparison for the CDM model. Note that since the quadratic Doppler effect carries a spectral distortion of $(\Delta T/T)_{RJ} = -2y$, we have multiplied the power by a factor of 4 to correspond to the case where the Rayleigh-Jeans temperature is measured. The quadratic Doppler effect is never dominant in this model.

$\mathcal{O}([\Theta_0 - \Theta]v_b)$ Quadratic Doppler Suppression

As discussed in §2.2.2, the quadratic Doppler effect ceases to operate once the photons are isotropic in the baryon rest frame. If the optical depth within a coherence scale of the baryon velocity $\mathbf{v}_b(\mathbf{x})$ is high, then the CMB will possess a dipole $\Theta - \Theta_0$ of exactly $\mathbf{v}_b(\mathbf{x})$. This will cancel any further contributions from the quadratic Doppler effect. However, in the small scale diffusion limit, by definition the optical depth never reaches unity in a coherence scale. The critical division is the horizon scale at optical depth unity, *i.e.* last scattering. In the mode-coupling integral, if the source of the contributions arise from larger wavelengths than this, they will be cancelled by the $\mathcal{O}([\Theta_0 - \Theta]v_b)$ term. This can only make the small quadratic Doppler contribution even smaller.

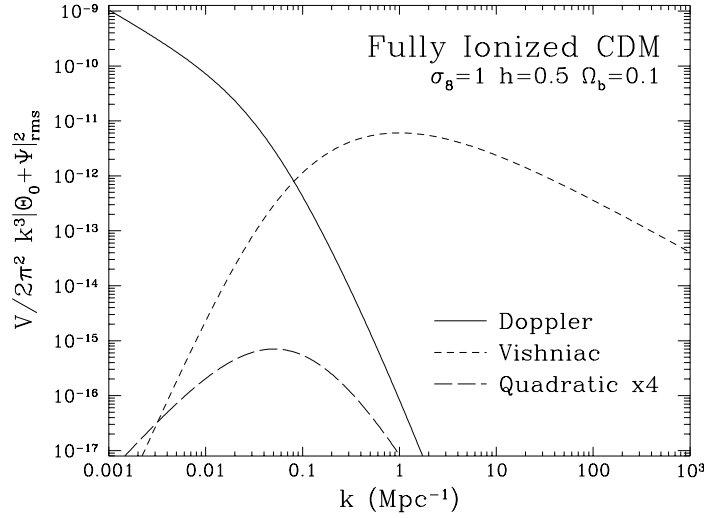


Figure 7.10: Quadratic Doppler Effect

Spatial power spectrum of the CMB for the first order Doppler, Vishniac and quadratic Doppler effects in a CDM model. The quadratic effect is multiplied by 4 to account for the spectral distortion in the Rayleigh-Jeans regime but never dominates.

$\mathcal{O}([\Theta_0 - \Theta]\Delta_b)$ Vishniac Suppression

The same suppression mechanism works for the Vishniac effect. Recall that the Vishniac effect arises since small scale overdensities can possess bulk velocities along the line of sight. The increased probability of scattering off overdense regions causes a small scale temperature variation from the Doppler shift. If the optical depth across the coherence scale of the bulk velocity is high, then all the photons will have scattered. Since further scattering does not affect the distribution, the increased probability of rescattering in overdense regions has no effect. In other words, a dipole $\Theta - \Theta_0$ has already been generated, such that the $\mathcal{O}([\Theta - \Theta_0]\Delta_b)$ term exactly cancels with the Vishniac $v_b\Delta_b$ term. Again one must check whether the Vishniac effect arises from bulk flows smaller or larger than the horizon at last scattering. By inserting cutoffs in the mode coupling integral equation (7.33), one can show that they arise from smaller scales for the range of power law spectra usually considered in the CDM and PIB models.

Mixed Order Terms

It is possible that first and third order terms couple in the rms. We have shown that the parallel and perpendicular components of the Doppler effect separate and add in

quadrature for C_ℓ (see [82] for the k -space proof). Since the first order contribution only possesses a parallel part, the mixed effect will only couple with the parallel third order term. However, this term is again severely suppressed by cancellation. The mixed order Doppler effect can therefore be entirely ignored.

7.3 Beyond Perturbation Theory: A Survey

*To acknowledge, mark out, study, assess,
Divide, discriminate, compete, and dispute.
These are our eight powers.
What is outside the cosmos, acknowledge but do not study.
What is within the cosmos, study but do not assess
What is a matter of record, assess but do not dispute.*

—Chuang-tzu, 2

Beyond the realm of linear calculations lies a plethora of higher order effects that are highly sensitive to assumptions about structure formation. Modeling and N-body simulations are needed to estimate their effects. Consequently, a full study of these individual effects is beyond the scope of this chapter. Instead, we survey the literature on these subjects and provide order of magnitude estimates where possible. Most of these effects are small in the degree to arcminute regime where one hopes that primary anisotropies will yield important cosmological information. Others such as the cluster Sunyaev-Zel'dovich effect and foreground sources in the galaxy may be filtered out by spectral information and object identification.

Cluster Sunyaev-Zel'dovich Effect

As pointed out by Sunyaev and Zel'dovich [162] clusters can induce anisotropies in the CMB from Compton scattering off electrons in the hot cluster medium. These hot electrons transfer energy to the CMB, leading to temperature anisotropies *and* spectral distortions in the CMB (see §3.2.1). The frequency dependence can be used to separate its signal from the primary anisotropy.

For a typical cluster of $T_e \simeq 1-10\text{keV}$ and a typical optical depth of $\tau \simeq 0.1-0.01$, the effect is of order $(\Delta T/T)_{RJ} = -2y \simeq 10^{-5} - 10^{-3}$. Of course, the rms fluctuation on a random patch of the sky will be much lower than this. Much effort has been expended to estimate the fluctuations caused by the SZ effect with varying results (e.g. [114, 112, 7, 33]).

Recently, empirical modelling of clusters has shown that the anisotropy at arcminutes is on the order of $(\Delta T/T)_{RJ} \lesssim 10^{-7}$ [27]. Moreover, the signal is in large part due to bright and easily identifiable clusters. If such known clusters are removed from the sample, the anisotropy drops to an entirely negligible level.

The peculiar velocity of a cluster also produces anisotropies via a Doppler shift of the scattered photons. This is the non-linear analogue of the Vishniac and patchy reionization effects. This process leads to no spectral distortions to first order and yields a true temperature fluctuation of $\Delta T/T = \mathcal{O}(\tau_c v_c)$ for an individual cluster, where the optical depth through the cluster is typically of order $\tau_c \simeq 0.1 - 0.01$ and its peculiar velocity $v_p \simeq \text{few} \times 10^{-3}$. Again there is hope that the signal can be removed by identifying bright clusters and perhaps even the thermal effect.

Rees-Sciama effect

Higher order corrections to the density evolution cause time dependence in the gravitational potentials from the Poisson equation. As pointed out by Rees & Sciama [136], this can cause a late ISW effect even in an $\Omega_0 = 1$ universe. The second order contribution has been shown to be negligibly small [115]. One can understand this by simple scaling arguments. Just as the first order late ISW contribution, this term suffers cancellation in power by $(k\delta\eta)^{-1}$ where $\delta\eta$ is now the time scale for change in the potential. The Poisson equation relates potentials to densities via a factor $(k\eta)^{-4}$ and the mode coupling volume factor yields k^3 . Thus the effect scales as $k^{-2}P(k)$ and will be small in comparison to even the minimal Vishniac effect if the mode coupling integrals behave similarly.

The fully non-linear case has been estimated using N-body simulations and power spectrum techniques [149]. In the standard CDM model, non-linear contributions dominate over the primary fluctuations only at $\ell \gtrsim 5000$ and are thus smaller than the minimal Vishniac effect. Ray tracing techniques corroborate these results by showing that fluctuations are at the 10^{-7} level at degree scales [167].

Gravitational Lensing

The presence of potential fluctuations gravitationally lenses the CMB and changes the projection of temperature inhomogeneities into anisotropies. Lensing neither generates or erases power but merely redistributes it in angles. The magnitude and sense of the effect

is somewhat dependent on the model for structure formation, including the assumptions for non-linear clustering. This has led to some seemingly inconsistent results in the literature (e.g. [14, 34, 143, 166, 108]). Recently Seljak [148] has shown that for CDM, and indeed most realistic scenarios of structure formation, the effect is small above the arcminute scales and above. At arcminute scales, it smooths out features such as the acoustic peaks at the few percent level in power.

Galactic Foreground Contamination

Though not a part of the cosmic microwave *background*, galactic foreground contamination contributes to anisotropies at microwave frequencies. This may make the extraction of information from the primary signal extremely difficult at small angular scales. Typical sources such as synchrotron, bremsstrahlung and dust emission can be identified by their spectral signature with multifrequency experiments (see *e.g.* [19, 9]). Near 100 GHz, one expects that synchrotron and bremsstrahlung will have already died away, whereas dust has not yet reached its peak. However, a sensitivity in the $\Delta T/T \lesssim 10^{-6}$ range will be necessary to extract some of the information encoded in the primary signal (see Appendix A.3). It may be however that even with full sky coverage from the next generation of satellite experiments only a small fraction containing the clean patches will be useful for observing the structure of primary anisotropies at this level. Clearly further work is needed on this important subject, but it may be that we will only know the full story once the next generation of CMB satellites have flown and taken data.

7.4 Final Thoughts

What goes on being hateful about analysis is that it implies that the analyzed is a completed set. The reason why completion goes on being hateful is that it implies everything can be a completed set.

–Chuang-tzu, 23

We have endeavored to cover all of the major sources of primary and secondary anisotropies in the CMB known to date. Still, there is no doubt that nature will continue to surprise us with the unexpected. In the end, despite the theory developed here, the ultimate answers can only be obtained through observations. Currently, several groups are testing long duration balloon flights in the hope that they will be able to measure anisotropies across a substantial fraction of the sky at degree resolutions. The experimental challenge to

eliminate atmospheric noise and sidelobe contamination is formidable (see *e.g.* [178]). Space based missions, for which these problems can be avoided, are now under consideration. A mission of this kind can essentially obtain cosmic variance limited measurements of the anisotropy spectrum down to ten arcminutes with a wide frequency coverage. With such data, one can realistically hope to measure all the classical cosmological parameters, the curvature K , the matter content $\Omega_0 h^2$, the cosmological constant Ω_Λ , the baryon content $\Omega_b h^2$ and possibly even the gravitational wave background and neutrino mass (see Appendix A.3.3 and A.3.4). The frequency coverage could allow measurements of the thermal SZ effect in a large number of clusters and yield a calibration of the distance scale and so measure the expansion rate h itself (see *e.g.* [13]). Combined with large scale structure measurements, the anisotropy data would provide important information on the model for structure formation as well as consistency tests for the gravitational instability scenario itself. Perhaps even more exciting is the chance that new phenomena, either cosmological or astrophysical, will be detected with all sky maps in the new frequency bands. Until such a mission flies, we can only guess at the possibilities.

Rather than go toward what suits you, laugh. Rather than acknowledge it with your laughter, shove it from you. Shove it from you and leave the transformation behind, then you will enter the unity of the featureless sky.

—Chuang-tzu, 6